Hydrogen Evolution Catalysts

Deutsche Ausgabe: DOI: 10.1002/ange.201508505
Internationale Ausgabe: DOI: 10.1002/anie.201508505

Phosphorus-Doped Carbon Nitride Tubes with a Layered Micro-nanostructure for Enhanced Visible-Light Photocatalytic Hydrogen Evolution

Shien Guo, Zhaopeng Deng, Mingxia Li, Baojiang Jiang, Chungui Tian, Qingjiang Pan, and Honggang Fu**

Abstract: *Phosphorus-doped hexagonal tubular carbon nitride (P-TCN) with the layered stacking structure was obtained from a hexagonal rod-like single crystal supramolecular precursor (monoclinic, C2/m). The production process of P-TCN involves two steps: 1) the precursor was prepared by self-assembly of melamine with cyanuric acid from in situ hydrolysis of melamine under phosphorous acid-assisted hydrothermal conditions; 2) the pyrolysis was initiated at the center of precursor under heating, thus giving the hexagonal P-TCN. The tubular structure favors the enhancement of light scattering and active sites. Meanwhile, the introduction of phosphorus leads to a narrow band gap and increased electric conductivity. Thus, the P-TCN exhibited a high hydrogen evolution rate of 67 μmol h^{-1} (0.1 g catalyst, $\lambda > 420$ nm) in the presence of sacrificial agents, and an apparent quantum efficiency of 5.68 % at 420 nm, which is better than most of bulk g-C_3N_4 reported.*

Graphitic carbon nitride (g-C_3N_4, labeled GCN), as a metal-free organic semiconductor, has attracted increasing attention because it possesses high thermal and chemical stability and an appealing electronic structure.[1] These unique properties of GCN allow for its diverse applications, such as photocatalytic hydrogen evolution, the oxygen reduction reaction (ORR), and oxygen evolution reaction (OER).[2–4] Bulk GCN obtained by the direct thermal polymerization process generally yields relatively low surface areas and less active sites for GCN, which significantly restricts its applications.[5] Additionally, the quantum efficiency of GCN in the visible light region needs to be further improved. The fabrication of hierarchical micro-nanostructures and heterogeneous element doping for GCN are two effective methods to solve the above problems. Typically, various kinds of micro-nanostructure GCN, including porous GCN, sphere GCN, and tubular GCN, were obtained through a hard-templating approach.[6,7] Nevertheless, this type of templating is time- and cost-inefficient, for it requires environmentally hazardous reagents to remove the template and prohibits further functionalization. Besides that, the chemical doped GCN with foreign elements, such as phosphorus and sulfur, can tune the energy band structure and conductivity of GCN, thus enhancing the visible-light photocatalytic quantum efficiency as well as improving their surface properties of GCN.[8] This means that the GCN with novel hierarchical micro-nanostructure and simultaneous nonmetal element doping by the template-free method is highly desirable but poses challenges.

To date, self-assembled supermolecular precursors by hydrogen bonding among molecules have emerged as a potential selection to prepare specially-shaped micro-nano materials, as hydrogen bonding has strong direction and saturation.[9] The ordered and hollow GCN structures had been synthesized using the cyanuric acid-melamine complex as a starting material.[10] The GCN microspheres and microsheets were also prepared using similar method by controlling precipitation temperature and selecting proper organic solvents.[11] The supramolecular precursors mentioned above were mainly produced by the assembly of two or more components under organic solvents. Undoubtedly, use of water solvent is more beneficial to molecule self-assembly based on hydrogen bonding, forming the stable, large-sized, and regular supramolecular precursors. It is well known that melamine could be transformed into cyanuric acid at a suitable pH value.[12] It would be desirable that supramolecular precursor can be synthesized in situ from a single melamine molecular source using acidic aqueous solution like phosphorous acid. The phosphorous acid not only could adjust pH value to prompt the hydrolysis of melamine into cyanuric acid, but also provide potential P source for the P-doping on GCN. Thus, we chose melamine and phosphorous acid as starting materials to produce the P-doped carbon nitride in situ with special hierarchical micro-nanostructure.

Herein, the fabrication process of phosphorus-doped hexagonal tubular carbon nitride (P-TCN) is shown as Scheme 1 (experimental details are given in the Supporting Information). Simply, melamine and phosphorous acid was dissolved in deionized water under heating. Then, under phosphorous acid assisted hydrothermal conditions (pH 1–3), the melamine was partly hydrolyzed in situ into cyanuric acid. Then the regular and stable hexagonal cylinder precursors were finally prepared through the molecule self-assembly between melamine and cyanuric acid (for the main reactions in the synthesis, see the Supporting Information, Scheme S1). Simultaneously, the phosphorous acid molecules could adsorb on the surface of precursor. After the thermal treatment, P

[*] S. Guo, Dr. Z. Deng, Dr. M. Li, Dr. B. Jiang, Prof. C. Tian, Prof. Q. Pan, Prof. H. Fu
Key Laboratory of Functional Inorganic Material Chemistry, Ministry of Education of the People's Republic of China, Heilongjiang University
Harbin 150080 (P.R. China)
E-mail: jiangbaojiang88@sina.com
fuhg@vip.sina.com

Supporting information for this article is available on the WWW under http://dx.doi.org/10.1002/anie.201508505.

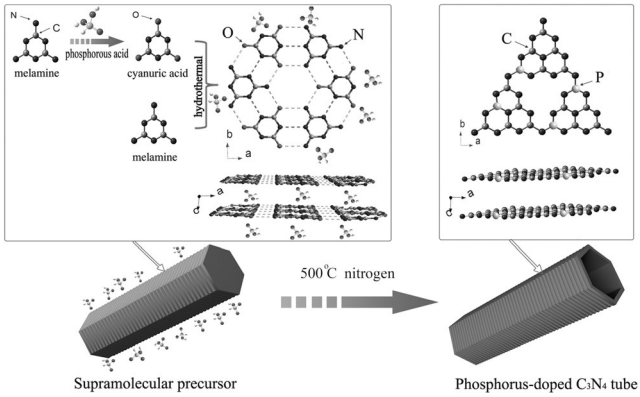

Scheme 1. The formation process of phosphorus-doped tubular carbon nitride.

from phosphorous acid squeezed into the GCN skeleton and the P-TCN was formed. It exhibited enhanced visible-light photocatalytic properties owing to the hierarchical micro-nanostructure and the P doping of GCN.

As shown in SEM images, supramolecular precursors for P-TCN (pH 1) possess a hexagonal rod structure with a length up to 300–500 μm and a diameter of 60–100 μm (Figure 1 a). A high-magnification image (Figure 1 b) reveals that the hexagonal rod precursors are composed of numbers of two-

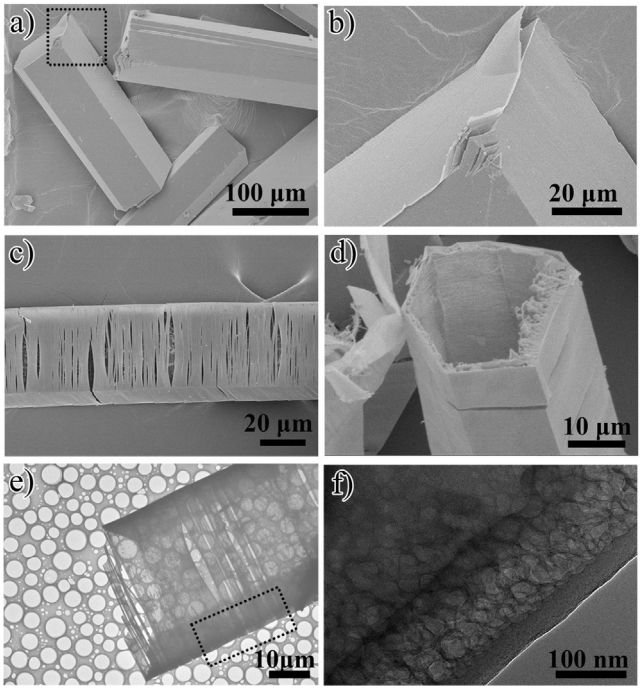

Figure 1. a), b) SEM images of supramolecular precursor, c), d) SEM images of P-TCN (PH = 1), and e), f) TEM images of P-TCN (pH 1).

dimensional sheets. Then the supramolecular complex precursor was analyzed by a single-crystal X-ray diffractometer (Supporting Information, Figure S1). The analysis results show that the melamine and cyanuric acid are held together by multiple hydrogen bonds in the same plane, yielding the hexamer, similar to previous reports.[9c] The cyanuric acid is from the partial in situ hydrolysis of melamine. The partial conversion of melamine into cyanuric acid and gradual formation of the supramolecular precursor are confirmed by FTIR spectroscopy (Supporting Information, Figures S2, S3) and XRD (Figures S4, S5). Meanwhile, the planar sheets consisting of condensed tri-s-triazine units are stacked in a perpendicular direction to the sheets via π–π interactions (the interlayer space is 3.224 Å), the structure being exactly as analyzed by SEM. Furthermore, the single crystal data and structure refinement for supramolecular precursor are also shown in the Supporting Information, Table S1. It is noted that the elemental analysis mapping (Supporting Information, Figure S6) show the homogeneous distribution of C, N, O and P elements. The presence of P should be from the adsorption of P-containing species on the supramolecular structure because single-crystal data does not display any P-containing species within supramolecular framework. A series of control experiments (Supporting Information, Figures S5, S7, S8) confirm that the reaction of melamine with cyanuric acid is slow. Once the cyanuric acid is formed in situ, the remaining melamine can react with cyanuric acid to form a supramolecular structure rapidly owing to the strong interactions. The phosphorous acid cannot be incorporated into the framework because of its weak interaction with malamine; it can only adsorb on the surface of the supramolecular structure. After polycondensation at 500 °C for 4 h, the transition from hexagonal rod to hexagonal tube has occurred as shown in Figure 1 c,d. It is clear that tubular external morphology of typical sample P-TCN (pH 1) is well maintained during the polycondensation, which is distinctly different from that of bulk GCN (Supporting Information, Figure S9 b). Moreover, the carbon nitride obtained from the pyrolysis of the precursor that is prepared in the absence of phosphorous also has irregular morphology (Supporting Information, Figure S9 d). These results confirm that the presence of phosphorous acid and the slow-release of cyanuric acid by the in situ hydrolyzation of melamine are very important for the formation of P-TCN. The similar tubular structures are also obtained at pH 2 or pH 3 (Supporting Information, Figure S10). Subsequent inestigations mainly focus on the typical sample P-TCN (pH 1). In Figure 1 e,f, the TEM measurements further confirmed that the desired hexagonal tube is successfully obtained. Additionally, the structural shrinkage leads to the formation of pores of 40–60 nm embedded in the tube wall of P-TCN. It can be expected that this micro-nanostructure will enhance the accessibility of catalytic sites. To deepen understanding of the formation mechanism of P-TCN, TGA-MS was conducted (Supporting Information, Figure S11 a,b). The formation of hexagonal tubes was mainly due to the release of gas, including NH_3, NO_2, NO, N_2O/CO_2, PH_3, and P, after pyrolysis of the supramolecular complex. These results are different from the pyrolysis of melamine (Supporting Information, Figure S12). The supramolecular precursor for carbon nitride tube was also analyzed by the TGA-MS (Supporting Information, Figure S11 c,d). For the supramolecular precursor, a high density of defects probably existed at the center of the hexagonal rod because of quickly crystallizing at the early stage of hydrothermal reaction (Supporting Information, Figure S13). The phosphorous acid adsorbed on surface of

precursor will also further strengthen its surface stability. Therefore, the pyrolysis or etching of precursor starts at the center of hexagonal rod, and gradually extends outward to form tube-like structure. Moreover, the speculation is also further evidenced by a series of SEM images (Supporting Information, Figure S14).

The TGA-MS results suggest that the release of phosphorous species during the synthesis of P-TCN, while there is still part of phosphorous species has been successfully introduced into the GCN lattice, as shown in elemental mapping images (Supporting Information, Figure S15). During the synthesis of P-TCN, phosphorous acid plays a key role like accelerating dissolution and hydrolysis of melamine, and stabilizing the precursor framework because of its acid–base interactions with melamine. Then the P modified precursor was further condensed under 500 °C under nitrogen, resulting in the P-TCN. As XRD patterns show (Figure 2a), the (002) peak centered at 27.7° becomes

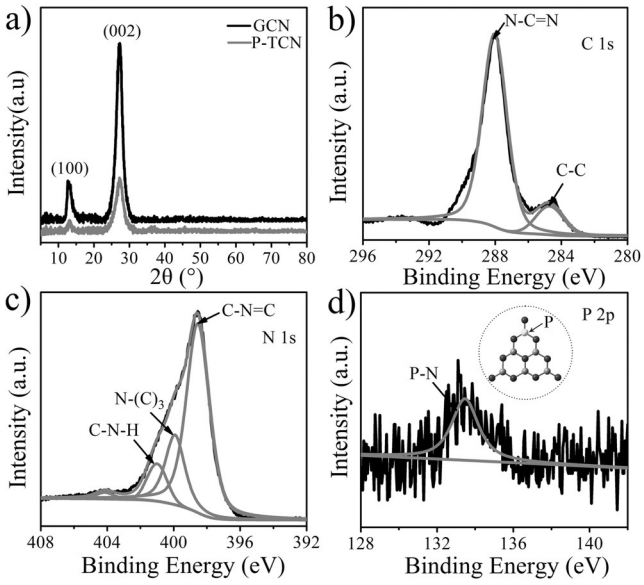

Figure 2. a) XRD patterns and b)–d) high-resolution XPS spectra of b) C 1s, c) N 1s, and d) P 2p that are obtained from P-TCN (pH 1).

broader and weaker and shifts to slightly lower scattering angles compared with the GCN, indicating the evident size-dependent properties of tube structure.[13] The specific surface area of P-TCN is 22.95 $m^2 g^{-1}$, which is about 7 times than that of GCN at 3.73 $m^2 g^{-1}$ (Supporting Information, Figure S16). P-TCN with large specific surface areas could provide more surface active sites. With no doubt, the special micro-nano-structure structure and introduced P heteroatom are expected to not only change the optical and electronic band structure, but also the charge-transfer efficiency of the GCN.

Further detailed electronic structures and chemical environment of C, N, and P elements in the sample P-TCN were analyzed with X-ray photoelectron spectroscopy (XPS) measurements. In the C 1s spectrum (Figure 2b), the mainly carbon species centering at 284.6 eV and 288.0 eV are assigned to the graphitic carbon (C–C) and the sp^2-hybridized carbon in the *N*-containing aromatic ring (*N*–C=N), respectively.[14] For the N 1s spectrum (Figure 2c), the small peak located at 404.2 eV is attributed to the positive charge localization in heterocycles; the big one starting from 396.4 eV to 402.7 eV can be deconvoluted into three peaks, including 398.4 eV for sp^2-hybridized nitrogen in triazine rings (C–N=C), 400.0 eV for tertiary nitrogen *N*-$(C)_3$ groups and 400.9 eV for amino functions carrying hydrogen (C–N–H). The peak of the amino carrying N species (400.9 eV) is found to be much higher than that in GCN (401.6 eV; Supporting Information, Figure S17), which is attributed to the special surface structure.[15] Furthermore, the shift of peak position also suggests the electron structure change for P-TCN. The peak of P 2p binding energy is centered at 133.5 eV, which is typical for P–N coordination (P–C bonding would be 1–2 eV lower), indicating that P most probably replaces C in triazine rings to form P–N bonds (Figure 2d).[16] Furthermore, the NMR investigations of P-TCN on the ^{31}P show signals between 10 and −20 ppm, which further prove the P doped in framework (Supporting Information, Figure S18).[16] The structure of the P-TCN sample is also confirmed by FTIR spectra (Supporting Information, Figure S19). The sharp peak at 802 cm^{-1} is caused by the breathing vibration of the triazine units.[8a] One new band at around 950 cm^{-1} is attributed to the P–N stretching mode,[8b] implying a certain amount of P incorporation, consistent with the EDS and XPS results. Compared with the C element, the doped P element possesses more electrons which will change the band structures of GCN and improve its electric conductivity. The element content of P is obtained from XPS analysis (Supporting Information, Table S2) and elemental analysis (Supporting Information, Table S3). The percentage of P from the elemental analysis is 1.21 wt% for P-TCN (pH 1).

The optical properties and band structures of the samples were analyzed by UV/Vis light absorption spectra and XPS valence band spectra. The formation of hexagonal tube increases the light absorption of P-TCN over the entire wavelength range, which is primarily due to the multiple reflections of incident light within the micro-nanostructure tube (Figure 3a).[17] The apparent color changed from pale yellow (GCN) to brown (P-TCN) (Supporting Information, Figure S20) is ascribed to the incorporation of P element into GCN matrix. Moreover, an evident shift of photoabsorption edge from 450 nm to 486 nm is observed for P-TCN. The corresponding band gap energy decreases from 2.67 eV (GCN) to 2.55 eV (P-TCN), which is consistent with previous report.[8] Then the valence band (VB) (Figure 3b) edge potential of P-TCN and GCN were measured by the XPS valence band. The VB energy levels of P-TCN and GCN were determined to be 1.44 eV and 1.67 eV, respectively. Compared with that of GCN, the VB of P-TCN shifts by 0.23 eV indicating that the electronic structure is altered owing to the P doping. Apparently, the conduction band (CB) edge of GCN and P-TCN were determined to be −1.0 eV and −1.11 eV, respectively. The CB of P-TCN shifts to more negative values can be attributed to the quantum confinement effects induced by hierarchical micro-nanostructure. The previous calculation results also show that P doping can increase the dispersion of the contour distribution of HOMO and LUMO, which improves the carrier mobility.[18] And this

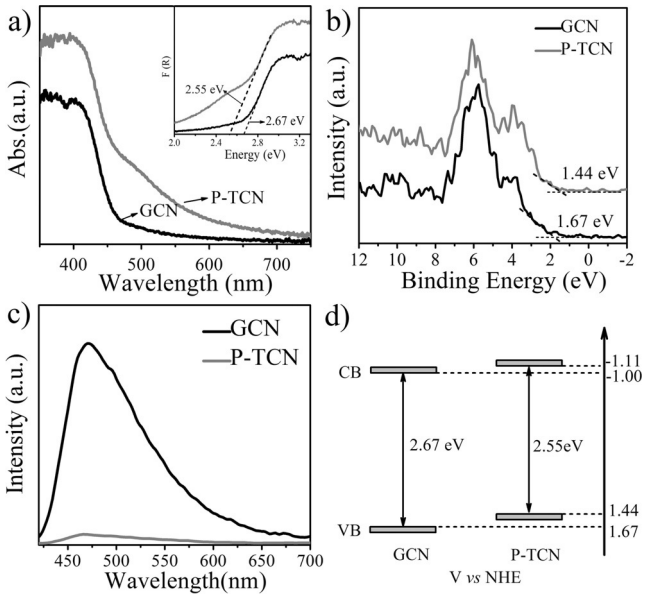

Figure 3. a) UV/Vis light absorption spectra and band gap energies (inset), b) XPS valence band spectra, c) photoluminescence spectra (400 nm excitation at room temperature), and d) band structure alignments of GCN and P-TCN (pH 1), respectively.

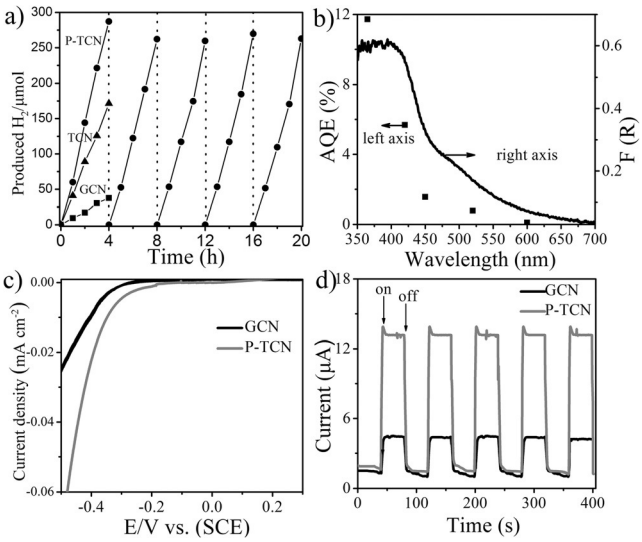

Figure 4. a) Time course of H_2 evolution for GCN, TCN, and P-TCN (pH 1) under visible light irradiation ($\lambda > 420$ nm), and b) wavelength-dependent AQE of H_2 evolution over 1 wt% Pt/P-TCN (left axis), UV/Vis light absorption spectra of P-TCN (right axis). c) Polarization curves of GCN and P-TCN; d) the photoelectrochemical responses of GCN and P-TCN under visible light irradiation.

kind of electronic band structure is beneficial, for which not only possesses the thermodynamically enhanced in photocatalytic reaction, but also inhibits electron–hole recombination. It is known that photoluminescence (PL) emission is useful to disclose the efficiency of electron-hole pairs trapping, migration, and transfer in semiconductor. In Figure 3c the photoluminescence intensity of P-TCN decreased drastically, and the decreased peak intensity further confirms a lower electron–hole recombination rate for P-TCN comparing with GCN. Then the band structure alignments of GCN and P-TCN are given in Figure 3d.

To illustrate the separation and dynamic processes of the photogenerated charge carriers, surface photovoltage spectroscopy (SPV) was performed, and the results are shown in the Supporting Information, Figure S21. Compared with GCN, the sample P-TCN has a weak SPV response. It is assumed that the P-TCN can easily capture photoinduced electrons and inhibits the recombination of photogenerated charges, which results in low surface net charges and a weak SPV response.[19] The evolution of electronic structure for P-TCN can be further revealed by the room-temperature electron paramagnetic resonance (EPR). A Lorentzian line is observed for GCN and P-TCN (Supporting Information, Figure S22), indicating the formation of unpaired electrons on π-conjugated CN aromatic rings.[20] However, the Lorentzian line for P-TCN can be greatly increased compared to the GCN, which is presumably due to the redistribution of electrons within P-TCN structure by the electron donation from the phosphorus species. These characterizations illustrate an encouraging result that P-TCN is favored for separation and migration of the photoinduced charge carriers, resulting in enhanced visible-light-derived hydrogen production performance.

Figure 4a shows a typical time course for hydrogen production using the GCN and P-TCN (pH 1) samples under visible-light irradiation ($\lambda > 420$ nm). As presented, the average hydrogen evolution rate of the P-TCN is 67 μmol h^{-1}, which is about seven times that of GCN (9 μmol h^{-1}). No hydrogen was detected in the dark test reaction (Supporting Information, Figure S23). Meanwhile, other P-TCN samples from different pH value and the TCN also exhibits high photocatalytic activity, indicating hexagonal tubes with a micro-nanostructure is beneficial for hydrogen evolution. Furthermore, the increase of P level within P-TCN could also improve its photocatalytic performance. The hydrogen production reaction was allowed to proceed for a total of 20 hours with intermittent degassing of the reaction every 4 hours (Supporting Information, Figure S24). Under the continuous hydrogen evolution, a total amount of 1.339 mmol H_2 is produced without noticeable deterioration of the activity, which suggests the high stability of P-TCN catalyst against photocorrosion. The P-TCN catalyst demonstrates high activity for photocatalytic hydrogen evolution based on its appropriate band alignments and unique micro-nanostructure. Figure 4b gives the apparent quantum efficiency (AQE) values for H_2 evolution of the P-TCN catalyst under various monochromatic light irradiation conditions. As can be seen, the variation tendencies of AQE curves are similar to their UV/Vis light absorption spectra. P-TCN catalyst gives high AQE in a range of 400–450 nm and the AQE value at 420 nm is estimated to be about 5.68%. This better photocatalytic performance for P-TCN should be attributed to the well-organized hexagonal tube frameworks; moreover, P element doping narrows the band gap and prompt the charge separation. After the photocatalytic reaction, the catalyst was recycled and then was characterized by XRD and FTIR, respectively (Supporting Information, Figure S25). Indeed, there is virtually no noticeable alternation in the structure of the catalyst before and after the reaction, again reflecting the robust nature of P-TCN.

To further illustrate the enhanced electron transfer in the P-TCN, photoelectrochemical measurements were conducted in a typical three-electrode cell (Figure 4c). Linear sweep voltammetry (LSV) measurements were performed under visible light irradiation. The observed cathodic current in the range of −0.2 to −0.4 V versus SCE (−0.6 to −0.9 V vs. RHE) can be ascribed to the hydrogen evolution reaction (HER). Compared to GCN, P-TCN shows a much higher catalytic activity. The enhanced catalytic capability was corroborated by the photocurrent measurements. Figure 4d shows a comparison of the photocurrent-time curves for the above samples with typical on–off cycles of visible light irradiation. An enhanced photocurrent response for P-TCN is generated, which is nearly three times higher than that of the pristine GCN, strongly illustrating that the mobility of the photoexcited charge carriers is promoted. Additionally, the Nyquist plots for P-TCN catalysts exhibit low charge transfer resistance as compared to those of GCN (Supporting Information, Figure S26).

In conclusion, through phosphorous acid-assisted hydrothermal method, partially hydrolysis of melamine into cyanuric acid leads to the formation of melamine–cyanuric acid supramolecular precursor. Then the hexagonal P-TCNs with the micro-nanostructure are obtained from supramolecular precursor after thermal treatment. The hexagonal tube with the layered stack structure significantly increases its specific surface area; as a result, the density of active sites is augmented. Moreover, the introduction of phosphorus decreases the band gap energy, increases the electric conductivity, and suppresses the recombination of photogenerated electron–hole pairs, thus improving the visible-light photocatalytic efficiency for the hydrogen evolution in the presence of sacrificial agents. The hexagonal carbon nitride tube structure is also good carrier material for nanocomposite with specified dimension and chemical functionality.

Acknowledgements

This work was supported by the NSFC of China (21031001, 21371053, 51372071, and 21571054), the Program for Innovative Research Team in University (IRT-1237).

Keywords: carbon nitride · micro-nanostructure · nanotubes · phosphorus doping · photocatalytic hydrogen evolution

How to cite: *Angew. Chem. Int. Ed.* **2016**, *55*, 1830–1834
Angew. Chem. **2016**, *128*, 1862–1866

[1] a) X. C. Wang, K. Maeda, A. Thomas, K. Takanabe, G. Xin, J. M. Carlsson, K. Domen, M. Antonietti, *Nat. Mater.* **2009**, *8*, 76–80; b) J. Liu, Y. Liu, N. Y. Liu, Y. Z. Han, X. Zhang, H. Huang, Y. Lifshitz, S. T. Lee, J. Zhong, Z. H. Kang, *Science* **2015**, *347*, 970–974.

[2] a) R. Kuriki, K. Sekizawa, O. Ishitani, K. Maeda, *Angew. Chem. Int. Ed.* **2015**, *54*, 2406–2409; *Angew. Chem.* **2015**, *127*, 2436–2439; b) X. H. Li, X. C. Wang, M. Antonietti, *ACS Catal.* **2012**, *2*, 2082–2086.

[3] a) S. Yang, X, Feng, X. Wang, K. Mullen, *Angew. Chem. Int. Ed.* **2011**, *50*, 5339–5343; *Angew. Chem.* **2011**, *123*, 5451–5455; b) Y. Zheng, J. Liu, J. Liang, M. Jaroniec, S. Z. Qiao, *Energy Environ. Sci.* **2012**, *5*, 6717–6774.

[4] S. Yang, Y. Gong, J. Zhang, L. Zhan, L. Ma, Z. Fang, R. Vajtai, X. Wang, P. M. Ajayan, *Adv. Mater.* **2013**, *25*, 2452–2456.

[5] a) X. Chen, S. Shen, L. Guo, S. Mao, *Chem. Rev.* **2010**, *110*, 6503–6570; b) A. Kudo, Y. Miseki, *Chem. Soc. Rev.* **2009**, *38*, 253–278.

[6] a) J. S. Zhang, M. W. Zhang, C. Yang, X. C. Wang, *Adv. Mater.* **2014**, *26*, 4121–4126; b) E. Z. Lee, Y.-S. Jun, W. H. Hong, A. Thomas, M. M. Jin, *Angew. Chem. Int. Ed.* **2010**, *49*, 9706–9710; *Angew. Chem.* **2010**, *122*, 9900–9904; c) Q. Li, J. P. Yang, D. Feng, Z. X. Wu, Q. L. Wu, S. S. Park, C.-S. Ha, D. Y. Zhao, *Nano Res.* **2010**, *3*, 632–642.

[7] a) Y. Y. Kang, Y. Q. Yang, L.-C. Yin, X. D. Kang, G. Liu, H.-M. Cheng, *Adv. Mater.* **2015**, *27*, 4572–4577; b) Y. P. Zhu, T. Z. Ren, Z. Y. Yuan, *ACS Appl. Mater. Interfaces* **2015**, *7*, 16850–16856; c) Q. Han, B. Wang, Y. Zhao, H. H. Cheng, L. T. Qu, *Angew. Chem. Int. Ed.* **2015**, *54*, 11433–11437; *Angew. Chem.* **2015**, *127*, 11595–11599.

[8] a) G. Liu, P. Niu, C. H. Sun, S. C. Smith, Z. G. Chen, G. Q. Lu, H. M. Cheng, *J. Am. Chem. Soc.* **2010**, *132*, 11642–11648; b) T. Y. Ma, J. Ran, S. Dai, M. Jaroniec, S. Z. Qiao, *Angew. Chem. Int. Ed.* **2015**, *54*, 4646–4650; *Angew. Chem.* **2015**, *127*, 4729–4733.

[9] a) G. M. Whitesides, J. P. Mathias, C. T. Seto, *Science* **1991**, *254*, 1312–1314; b) N. A. Wasio, R. C. Quardokus, R. P. Forrest, C. S. Lent, S. A. Corcelli, J. A. Christie, K. W. Henderson, S. A. Kandel, *Nature* **2014**, *507*, 86–89; c) A. Ranganathan, V. R. Pedireddi, C. N. R. Rao, *J. Am. Chem. Soc.* **1999**, *121*, 1752–1753; d) M. Shalom, M. Guttentag, C. Fettkenhauer, S. Inal, D. Neher, A. Llobet, M. Antonietti, *Chem. Mater.* **2014**, *26*, 5812–5818; e) T. Jordan, N. Fechler, J. S. Xu, T. J. K. Brenner, M. Antonietti, M. Shalom, *ChemCatChem* **2015**, *7*, 2826–2830; f) Y. Ishida, L. Chabanne, M. Antonietti, M. Shalom, *Langmuir* **2014**, *30*, 447–451.

[10] M. Shalom, S. Inal, C. Fettkenhauer, D. Neher, M. Antonietti, *J. Am. Chem. Soc.* **2013**, *135*, 7118–7121.

[11] Y.-S. Jun, J. Park, S. U. Lee, A. Thomas, W. H. Hong, G. D. Stucky, *Angew. Chem. Int. Ed.* **2013**, *52*, 11083–11087; *Angew. Chem.* **2013**, *125*, 11289–11293.

[12] K. Jutzi, A. M. Cook, R. Huitter, *Biochem. J.* **1982**, *208*, 679–684.

[13] J. H. Zhang, G. G. Zhang, X. F. Chen, S. Lin, L. Mohlmann, G. Dolega, G. Lipner, M. Antonietti, S. Blechert, X. C. Wang, *Angew. Chem. Int. Ed.* **2012**, *51*, 3183–3187; *Angew. Chem.* **2012**, *124*, 3237–3241.

[14] J. Zhang, M. Zhang, G. Zhang, X. Wang, *ACS Catal.* **2012**, *2*, 940–944.

[15] J. Zhang, F. Guo, X. Wang, *Adv. Funct. Mater.* **2013**, *23*, 3008–3012.

[16] Y. J. Zhang, T. Mori, J. H. Ye, M. Antonietti, *J. Am. Chem. Soc.* **2010**, *132*, 6294–6295.

[17] a) X. Wang, K. Maeda, X. Chen, K. Takanabe, K. Domen, Y. Hou, X. Fu, M. Antonietti, *J. Am. Chem. Soc.* **2009**, *131*, 1680–1684; b) K. Kailasam, J. D. Epping, A. Thomas, S. Losse, H. Junge, *Energy Environ. Sci.* **2011**, *4*, 4668–4671.

[18] X. G. Ma, Y. H. Lv, J. Xu, Y. F. Liu, R. Q. Zhang, Y. F. Zhu, *J. Phys. Chem. C* **2012**, *116*, 23485–23493.

[19] L. Q. Jing, Y. C. Qu, H. J. Su, C. H. Yao, H. G. Fu, *J. Phys. Chem. C* **2011**, *115*, 12375.

[20] a) J. Zhang, X. Chen, K. Takanabe, K. Maeda, K. Domen, J. Epping, X. Fu, M. Antonietti, X. Wang, *Angew. Chem. Int. Ed.* **2010**, *49*, 441–445; *Angew. Chem.* **2010**, *122*, 451–454.

Received: September 10, 2015
Revised: November 3, 2015
Published online: December 21, 2015

